Article:
Karageorghis, A, Lesnic, D and Marin, L (2016) The method of fundamental solutions for three-dimensional inverse geometric elasticity problems. Computers and Structures, 166. pp. 51-59. ISSN 0045-7949

https://doi.org/10.1016/j.compstruc.2016.01.010

The method of fundamental solutions for three-dimensional inverse geometric elasticity problems

A. Karageorghis[1,*], D. Lesnic[2,†], and L. Marin[3,4,‡]

[1]Department of Mathematics and Statistics, University of Cyprus/Πανεπιστήμιο Κύπρου,

P.O.Box 20537, 1678 Nicosia/Λευκωσία, Cyprus/Κύπρος

[2]Department of Applied Mathematics, University of Leeds, Leeds LS2 9JT, UK

[3]Department of Mathematics, Faculty of Mathematics and Computer Science,

University of Bucharest, 14 Academiei, 010014 Bucharest, Romania

[4]Institute of Solid Mechanics, Romanian Academy, 15 Constantin Mille, 010141 Bucharest, Romania

Abstract

We investigate the numerical reconstruction of smooth star-shaped voids (rigid inclusions and cavities) which are compactly contained in a three-dimensional isotropic linear elastic medium from a single set of Cauchy data (i.e. nondestructive boundary displacement and traction measurements) on the accessible outer boundary. This inverse geometric problem in three-dimensional elasticity is approximated using the method of fundamental solutions (MFS). The parameters describing the boundary of the unknown void, its centre, and the contraction and dilation factors employed for selecting the fictitious surfaces where the MFS sources are to be positioned, are taken as unknowns of the problem. In this way, the original inverse geometric problem is reduced to finding the minimum of a nonlinear least-squares functional that measures the difference between the given and computed data, penalized with respect to both the MFS constants and the derivative of the radial coordinates describing the position of the star-shaped void. The interior source points are anchored and move with the void during the iterative reconstruction procedure. The feasibility of this new method is illustrated in several numerical examples.

2000 Mathematics Subject Classification. Primary 65N35; Secondary 65N21, 65N38.

*Corresponding author. E-mail: andreask@ucy.ac.cy

†E-mail: amt5ld@maths.leeds.ac.uk

‡E-mails: marin.liviu@gmail.com; liviu.marin@fmi.unibuc.ro

Keywords: method of fundamental solutions, Cauchy-Navier equations of elasticity, inverse problems.

January 7, 2016

1 Introduction

In direct problems in solid mechanics, one has to determine the response of a system when the governing partial differential equations (equilibrium equations), the constitutive and kinematics equations, the initial and boundary conditions for the displacement and/or traction vectors and the geometry of the domain occupied by the solid are all known. However, if at least one of the above conditions is partially or entirely lacking, then one has a so-called inverse problem. Moreover, it is well-known that inverse problems are in general unstable, in the sense that small measurement errors in the input data may amplify significantly the errors in the solution, see e.g. [16]. Such inverse problems have been extensively studied, both theoretically and numerically, over the last three decades and an overview of these developments can be found in [10].

In the case of inverse geometric problems in solid mechanics, which represent an important subclass of inverse problems, the geometry of the domain occupied by the solid is not entirely known, however some additional information is available. More specifically, part of the boundary of the solution domain is not known but either the displacements or the tractions are known on this portion, whilst the remaining boundary is known and both displacement and traction measurements are available on it. The inverse geometric problems described above can be further subdivided into two subclasses, depending on the location of the unknown boundary, namely (i) identification of an unknown boundary or corrosion-type problems (the unknown boundary is a part of the outer boundary of the solution domain), see e.g. [27–29], and (ii) identification of voids, i.e. cavities and rigid inclusions (the unknown boundary is an inner boundary), see e.g. [12, 21–23].

There are important studies that are devoted to the latter subclass of inverse geometric problems in elasticity. Alessandrini et al. [1, 2] proved that the volume (size) of a rigid inclusion in an elastic isotropic body can be estimated by an easily expressed quantity related to work, depending only on the boundary traction and displacement. Morassi and Rosset [33] provided upper and lower bounds on the size of unknown defects, such as cavities or rigid inclusions, in an elastic body, from boundary measurements of tractions and displacements. Later, they considered the inverse problem of determining a rigid inclusion inside an isotropic elastic body from a single set of Cauchy data on the outer boundary and proved its uniqueness and conditional stability [34]. The

issue of uniqueness in determining cavities in a heterogeneous isotropic elastic medium in two dimensions was investigated by Ang et al. [4], who used the unique continuation for the isotropic Lamé system and geometric considerations. Ben Ameur et al. [8] developed a rather general approach for identifiability and local Lipschitz stability of cavities in two and three spatial dimensions in linear elasticity and thermo-elasticity. Ikehata and Itou [19] considered the reconstruction problem of an unknown polygonal cavity in a homogeneous isotropic elastic body and provided an extraction formula of the convex hull of the cavity using the enclosure method.

With respect to the numerical identification of voids in elasticity, most of the studies available in the literature are devoted to the two-dimensional case. A regularized boundary integral formulation for the detection of flaws in planar structural membranes from the displacement measurements given at some boundary locations and the applied loading was proposed in [9]. Hsieh and Mura [18] developed a combined boundary element method (BEM)-nonlinear optimization algorithm for the detection of both the location and the shape of an unknown cavity in an elastic medium. Mellings and Aliabadi [30] presented a dual boundary element formulation for the identification of the location and size of internal flaws in two-dimensional structures. Kassab et al. [24] and Ulrich et al. [37] investigated the non-destructive detection of internal cavities in the inverse elastostatic problem using the BEM. The level set method and a regularization technique related to the perimeter of the unknown inclusion were employed by Ben Ameur et al. [7] for the numerical reconstruction of a void from a single Cauchy data. We finally mention that some three-dimensional elastodynamic inverse problems have been solved using the BEM in [6, 11].

In recent years the method of fundamental solutions (MFS), originally proposed by Kupradze and Aleksidze [26] and introduced as a numerical method by Mathon and Johnston [31], has been used extensively for the numerical solution of inverse and related problems primarily due to its ease of implementation. An extensive survey of the applications of the MFS to inverse problems is provided in [20]. It appears that the MFS was used for the first time for the solution of inverse geometric problems in linear elasticity by Alves and Martins [3], who adapted to the detection of rigid inclusions or cavities in an elastic body the method of Kirsch and Kress [25]. The method of [3] decomposes the inverse problem into a linear and ill-posed part in which a Cauchy problem is solved using the MFS and a nonlinear part in which the unknown boundary of the void is sought as a zero level set for a rigid inclusion (or computed iteratively, in an optimization scheme for a class of approximating shapes, for a cavity). In contrast to this, Karageorghis et al. [21] adopted a fully nonlinear MFS in which the nonlinear and ill-posed parts are dealt with simultaneously using a nonlinear regularized minimization. The reconstructions

obtained using this latter method are more accurate than those obtained by decomposition methods, see e.g. [36].

The purpose of this paper is to extend to three-dimensional elasticity the two-dimensional analysis of [21], the same way we have done for the harmonic scalar case in [22, 23]. In particular, we extend the work of [23] to three-dimensional inverse geometric problems, see also [12]. The paper is organized as follows: Section 2 is devoted to the mathematical formulation of the inverse geometric problem investigated. The MFS discretization for this problem is described in Section 3, while the implementational details are given in Section 4. In Section 5, we investigate four examples. Finally, some concluding remarks and possible future work are provided in Section 6.

2 The Cauchy-Navier equations of elasticity

2.1 The problem

We consider the boundary value problem in a bounded domain $\Omega \subset \mathbb{R}^3$ for the Cauchy–Navier system of elasticity for the displacement $\boldsymbol{u}$ in the form (see e.g. [17])

$$\mu \Delta \boldsymbol{u} + \frac{\mu}{1-2\nu} \nabla \cdot \nabla \boldsymbol{u} = \boldsymbol{0} \quad \text{in} \quad \Omega, \tag{1a}$$

where $\mu > 0$ is the shear modulus and $\nu \in (0, 1/2)$ is the Poisson ratio, subject to the Dirichlet boundary conditions

$$\boldsymbol{u} = \boldsymbol{f} \quad \text{on} \quad \partial\Omega_2, \tag{1b}$$

and the homogeneous boundary conditions

$$\alpha \boldsymbol{u} + (1-\alpha)\boldsymbol{t} = \boldsymbol{0} \quad \text{on} \quad \partial\Omega_1, \tag{1c}$$

where α is 0 or 1. The inverse problem we are concerned with consists of determining not only the displacement $\boldsymbol{u}$, but also the unknown inclusion Ω_1 so that $\boldsymbol{u}$ satisfies the Cauchy-Navier equations (1a), given the Dirichlet data $\boldsymbol{f}$ in (1b), the homogeneous boundary condition (1c) and the Neumann traction measurements

$$\boldsymbol{t} = \boldsymbol{g} \quad \text{on} \quad \partial\Omega_2\,. \tag{1d}$$

In the above, $\Omega = \Omega_2 \backslash \Omega_1$, where $\overline{\Omega}_1 \subset \Omega_2$, is a bounded annular domain with boundary $\partial\Omega = \partial\Omega_1 \cup \partial\Omega_2$. The void Ω_1 may have many connected components, but Ω should be connected. Equation (1c), covers both

homogeneous Dirichlet ($\alpha = 1$, i.e. Ω_1 is a rigid inclusion) and Neumann ($\alpha = 0$, i.e. Ω_1 is a cavity) boundary conditions on $\partial\Omega_1$. In (1c), $\boldsymbol{t}$ represents the traction defined by

$$\boldsymbol{t} = \boldsymbol{\sigma}\boldsymbol{n} \quad \text{on} \quad \partial\Omega_2. \tag{2}$$

In (2), the outward normal unit vector to the boundary at the point (x_1, x_2, x_3) is denoted by $\boldsymbol{n}(x_1, x_2, x_3) = (\mathrm{n}_{x_1}, \mathrm{n}_{x_2}, \mathrm{n}_{x_3})$, whilst $\boldsymbol{\sigma}$ is the stress tensor given, in terms of the strain tensor $\boldsymbol{\varepsilon} = \big(\nabla\boldsymbol{u} + (\nabla\boldsymbol{u})^{\mathsf{T}}\big)/2$, by Hooke's law [17], namely

$$\boldsymbol{\sigma} = 2\mu\left[\boldsymbol{\varepsilon} + \frac{\nu}{1-2\nu}\mathrm{tr}(\boldsymbol{\varepsilon})\boldsymbol{I}\right] \quad \text{in} \quad \overline{\Omega}, \tag{3}$$

where $\boldsymbol{I}$ is the 3×3 identity matrix.

If the Dirichlet and Neumann data (1b) and (1d) are not identically zero, then the uniqueness of the solution pair $(\boldsymbol{u}, \Omega_1)$ of the inverse problem (1a)-(1d) holds, see [3].

3 The method of fundamental solutions (MFS)

In the application of the MFS to (1), we seek an approximation to the solution of the three-dimensional Cauchy-Navier equations of elasticity as a linear combination of fundamental solutions in the form [35]

$$\boldsymbol{u}_{NM}(\boldsymbol{a}^1, \boldsymbol{a}^2, \boldsymbol{b}^1, \boldsymbol{b}^2, \boldsymbol{c}^1, \boldsymbol{c}^2, \boldsymbol{\xi}^1, \boldsymbol{\xi}^2; \boldsymbol{x}) = \sum_{s=1}^{2}\sum_{n=1}^{N}\sum_{m=1}^{M} \boldsymbol{G}(\boldsymbol{\xi}_{n,m}^s, \boldsymbol{x})\big[a_{n,m}^s \; b_{n,m}^s \; c_{n,m}^s\big]^{\mathsf{T}}, \tag{4}$$

where $\boldsymbol{G}(\boldsymbol{\xi}, \boldsymbol{x}) = \big[G_{ij}(\boldsymbol{\xi}, \boldsymbol{x})\big]_{1\le i,j\le 3}$ is the fundamental solution matrix for the displacement vector in three-dimensional isotropic linear elasticity given by

$$\boldsymbol{G}(\boldsymbol{\xi}, \boldsymbol{x}) = \frac{1}{16\pi\mu(1-\nu)}\frac{1}{|\boldsymbol{x}-\boldsymbol{\xi}|}\left[(3-4\nu)\boldsymbol{I} + \frac{\boldsymbol{x}-\boldsymbol{\xi}}{|\boldsymbol{x}-\boldsymbol{\xi}|} \otimes \frac{\boldsymbol{x}-\boldsymbol{\xi}}{|\boldsymbol{x}-\boldsymbol{\xi}|}\right], \tag{5}$$

and the vectors $\boldsymbol{a}^s = \big[a_{1,1}^s, a_{1,2}^s, \ldots, a_{N,M}^s\big]$, $\boldsymbol{b}^s = \big[b_{1,1}^s, b_{1,2}^s, \ldots, b_{N,M}^s\big]$ and $\boldsymbol{c}^s = \big[c_{1,1}^s, c_{1,2}^s, \ldots, c_{N,M}^s\big]$, $s = 1, 2$, contain the unknown MFS coefficients. Similarly, from (2), (4) and (5), the tractions are approximated by [5]

$$\boldsymbol{t}_{NM}(\boldsymbol{a}^1, \boldsymbol{a}^2, \boldsymbol{b}^1, \boldsymbol{b}^2, \boldsymbol{c}^1, \boldsymbol{c}^2, \boldsymbol{\xi}^1, \boldsymbol{\xi}^2; \boldsymbol{x}) = \sum_{s=1}^{2}\sum_{n=1}^{N}\sum_{m=1}^{M} \boldsymbol{T}(\boldsymbol{\xi}_{n,m}^s, \boldsymbol{x})\big[a_{n,m}^s \; b_{n,m}^s \; c_{n,m}^s\big]^{\mathsf{T}} \tag{6}$$

where $\boldsymbol{T}(\boldsymbol{\xi}, \boldsymbol{x}) = \big[T_{ij}(\boldsymbol{\xi}, \boldsymbol{x})\big]_{1\le i,j\le 3}$ is the fundamental solution matrix for the traction vector in three-dimensional isotropic linear elasticity, whose components are given by

$$\begin{aligned} T_{1j}(\boldsymbol{\xi}, \boldsymbol{x}) = {} & \frac{2\mu}{1-2\nu}\left[(1-\nu)\frac{\partial G_{1j}}{\partial x_1}(\boldsymbol{\xi}, \boldsymbol{x}) + \nu\left(\frac{\partial G_{2j}}{\partial x_2}(\boldsymbol{\xi}, \boldsymbol{x}) + \frac{\partial G_{3j}}{\partial x_3}(\boldsymbol{\xi}, \boldsymbol{x})\right)\right]\mathrm{n}_{x_1}(\boldsymbol{x}) \\ & + \mu\left[\frac{\partial G_{1j}}{\partial x_2}(\boldsymbol{\xi}, \boldsymbol{x}) + \frac{\partial G_{2j}}{\partial x_1}(\boldsymbol{\xi}, \boldsymbol{x})\right]\mathrm{n}_{x_2}(\boldsymbol{x}) + \mu\left[\frac{\partial G_{1j}}{\partial x_3}(\boldsymbol{\xi}, \boldsymbol{x}) + \frac{\partial G_{3j}}{\partial x_1}(\boldsymbol{\xi}, \boldsymbol{x})\right]\mathrm{n}_{x_3}(\boldsymbol{x}), \quad j = 1, 2, 3, \end{aligned} \tag{7a}$$

$$T_{2j}(\boldsymbol{\xi},\boldsymbol{x}) = \frac{2\mu}{1-2\nu}\left[(1-\nu)\frac{\partial G_{2j}}{\partial x_2}(\boldsymbol{\xi},\boldsymbol{x}) + \nu\left(\frac{\partial G_{3j}}{\partial x_3}(\boldsymbol{\xi},\boldsymbol{x}) + \frac{\partial G_{1j}}{\partial x_1}(\boldsymbol{\xi},\boldsymbol{x})\right)\right]\mathrm{n}_{x_2}(\boldsymbol{x}) \\ + \mu\left[\frac{\partial G_{2j}}{\partial x_3}(\boldsymbol{\xi},\boldsymbol{x}) + \frac{\partial G_{3j}}{\partial x_2}(\boldsymbol{\xi},\boldsymbol{x})\right]\mathrm{n}_{x_3}(\boldsymbol{x}) + \mu\left[\frac{\partial G_{2j}}{\partial x_1}(\boldsymbol{\xi},\boldsymbol{x}) + \frac{\partial G_{1j}}{\partial x_2}(\boldsymbol{\xi},\boldsymbol{x})\right]\mathrm{n}_{x_1}(\boldsymbol{x}), \quad j=1,2,3, \tag{7b}$$

$$T_{3j}(\boldsymbol{\xi},\boldsymbol{x}) = \frac{2\mu}{1-2\nu}\left[(1-\nu)\frac{\partial G_{3j}}{\partial x_3}(\boldsymbol{\xi},\boldsymbol{x}) + \nu\left(\frac{\partial G_{1j}}{\partial x_1}(\boldsymbol{\xi},\boldsymbol{x}) + \frac{\partial G_{2j}}{\partial x_2}(\boldsymbol{\xi},\boldsymbol{x})\right)\right]\mathrm{n}_{x_3}(\boldsymbol{x}) \\ + \mu\left[\frac{\partial G_{3j}}{\partial x_1}(\boldsymbol{\xi},\boldsymbol{x}) + \frac{\partial G_{1j}}{\partial x_3}(\boldsymbol{\xi},\boldsymbol{x})\right]\mathrm{n}_{x_1}(\boldsymbol{x}) + \mu\left[\frac{\partial G_{3j}}{\partial x_2}(\boldsymbol{\xi},\boldsymbol{x}) + \frac{\partial G_{2j}}{\partial x_3}(\boldsymbol{\xi},\boldsymbol{x})\right]\mathrm{n}_{x_2}(\boldsymbol{x}), \quad j=1,2,3. \tag{7c}$$

The sources $(\boldsymbol{\xi}^s_{n,m})_{n=\overline{1,N},m=\overline{1,M},s=\overline{1,2}}$ are located outside the solution domain Ω, i.e. in $\Omega_1 \cup \left(\mathbb{R}^3\backslash\bar{\Omega}_2\right)$. In particular, the sources $(\boldsymbol{\xi}^1_{n,m})_{n=\overline{1,N},m=\overline{1,M}} \in \Omega_1$ are placed on a (moving) pseudo-boundary $\partial\Omega_1'$ similar (contraction) to $\partial\Omega_1$, while the sources $(\boldsymbol{\xi}^2_{n,m})_{n=\overline{1,N},m=\overline{1,M}} \in \mathbb{R}^3\backslash\overline{\Omega}_2$ are placed on a pseudo-boundary $\partial\Omega_2'$ similar (dilation) to $\partial\Omega_2$. In the MFS, taking the pseudo-boundary similar to the boundary yields, in general, improved results as has been demonstrated by Gorzelańczyk and Kołodziej [15]. In (4), the singularities $(\boldsymbol{\xi}^2_{n,m})_{n=\overline{1,N},m=\overline{1,M}}$ are *not* preassigned. Also, the sources $(\boldsymbol{\xi}^1_{n,m})_{n=\overline{1,N},m=\overline{1,M}}$ move with $\partial\Omega_1$, as will be described in the iterative process presented in the sequel. The fact that the locations of the pseudo-boundaries $\partial\Omega_1'$ and $\partial\Omega_2'$ are determined as part of the solution takes care of the inherent problem of optimally locating the sources in the MFS.

Without loss of generality, we shall assume that the (known) fixed exterior boundary $\partial\Omega_2$ is a sphere of radius R. As a result, the outer boundary collocation and source points are chosen as

$$\boldsymbol{x}^2_{k,\ell} = R\left(\sin\tilde{\vartheta}_k\cos\tilde{\phi}_\ell, \sin\tilde{\vartheta}_k\sin\tilde{\phi}_\ell, \cos\tilde{\vartheta}_k\right), \quad k=\overline{1,\widetilde{N}},\ \ell=\overline{1,\widetilde{M}}, \tag{8}$$

$$\boldsymbol{\xi}^2_{n,m} = \eta_{ext}\,R\left(\sin\vartheta_n\cos\phi_m, \sin\vartheta_n\sin\phi_m, \cos\vartheta_n\right), \quad n=\overline{1,N},\ m=\overline{1,M}, \tag{9}$$

respectively, where

$$\tilde{\vartheta}_k = \frac{\pi k}{\widetilde{N}+1},\ k=\overline{1,\widetilde{N}}, \quad \tilde{\phi}_\ell = \frac{2\pi(\ell-1)}{\widetilde{M}},\ \ell=\overline{1,\widetilde{M}},$$

and

$$\vartheta_n = \frac{\pi n}{N+1},\ n=\overline{1,N}, \quad \phi_m = \frac{2\pi(m-1)}{M},\ m=\overline{1,M},$$

and the (unknown) dilation parameter $\eta_{ext} \in (1,S)$, with $S>1$ prescribed.

We further assume that the unknown boundary $\partial\Omega_1$ is a smooth, star-like surface with respect to its centre which has unknown coordinates (X,Y,Z). This means that its equation in spherical coordinates can be written as

$$x = X + r(\vartheta,\phi)\sin\vartheta\cos\phi, \quad y = Y + r(\vartheta,\phi)\sin\vartheta\sin\phi, \quad z = Z + r(\vartheta,\phi)\cos\vartheta, \quad \vartheta\in(0,\pi), \quad \phi\in[0,2\pi), \tag{10}$$

where r is a smooth function with values in $(0, R)$. The discretised form of (10) for $\partial\Omega_1$ becomes

$$r_{n,m} = r(\vartheta_n, \phi_m), \quad n = \overline{1, N},\ m = \overline{1, M}, \tag{11}$$

and we choose the inner boundary collocation and source points as

$$\boldsymbol{x}^1_{n,m} = (X, Y, Z) + r_{n,m}\,(\sin\vartheta_n\cos\phi_m, \sin\vartheta_n\sin\phi_m, \cos\vartheta_n) \quad n = \overline{1, N},\ m = \overline{1, M}, \tag{12}$$

$$\boldsymbol{\xi}^1_{m,n} = (X, Y, Z) + \eta_{int}\, r_{n,m}\,(\sin\vartheta_n\cos\phi_m, \sin\vartheta_n\sin\phi_m, \cos\vartheta_n)\,, \quad n = \overline{1, N},\ m = \overline{1, M}, \tag{13}$$

where the (unknown) contraction parameter $\eta_{int} \in (0, 1)$.

4 Implementational details

The coefficients $\boldsymbol{a}^1 = \left(a^1_{n,m}\right)_{n=\overline{1,N},m=\overline{1,M}}$, $\boldsymbol{a}^2 = \left(a^2_{n,m}\right)_{n=\overline{1,N},m=\overline{1,M}}$, $\boldsymbol{b}^1 = \left(b^1_{n,m}\right)_{n=\overline{1,N},m=\overline{1,M}}$, $\boldsymbol{b}^2 = \left(b^2_{n,m}\right)_{n=\overline{1,N},m=\overline{1,M}}$, $\boldsymbol{c}^1 = \left(c^1_{n,m}\right)_{n=\overline{1,N},m=\overline{1,M}}$, $\boldsymbol{c}^2 = \left(c^2_{n,m}\right)_{n=\overline{1,N},m=\overline{1,M}}$ in (4), the radii $\boldsymbol{r} = (r_{n,m})_{n=\overline{1,N},m=\overline{1,M}} \in (0, R)$ in (11), the contraction and dilation coefficients $\eta_{int} \in (0, 1)$ and $\eta_{ext} \in (1, S)$ in (13) and (9), and the coordinates of the centre $\boldsymbol{C} = (X, Y, Z)$ so that $X^2 + Y^2 + Z^2 < R^2$ can be determined by imposing the boundary conditions (1b), (1c) and (1d) in a regularized least-squares sense. This leads to the minimization of the functional

$$\begin{aligned}
S(\boldsymbol{a}^1, \boldsymbol{a}^2, \boldsymbol{b}^1, \boldsymbol{b}^2, \boldsymbol{c}^1, \boldsymbol{c}^2, \boldsymbol{r}, \boldsymbol{\eta}, \boldsymbol{C}) &:= \sum_{n=1}^{\widetilde{N}}\sum_{m=1}^{\widetilde{M}} \left|\boldsymbol{u}_{NM}(\boldsymbol{a}^1, \boldsymbol{a}^2, \boldsymbol{b}^1, \boldsymbol{b}^2, \boldsymbol{c}^1, \boldsymbol{c}^2, \boldsymbol{\xi}^1, \boldsymbol{\xi}^2; \boldsymbol{x}^2_{n,m}) - \boldsymbol{f}^{\varepsilon}(\boldsymbol{x}^2_{n,m})\right|^2 \\
&+ \sum_{n=1}^{\widetilde{N}}\sum_{m=1}^{\widetilde{M}} \left|\boldsymbol{t}_{NM}(\boldsymbol{a}^1, \boldsymbol{a}^2, \boldsymbol{b}^1, \boldsymbol{b}^2, \boldsymbol{c}^1, \boldsymbol{c}^2, \boldsymbol{\xi}^1, \boldsymbol{\xi}^2; \boldsymbol{x}^2_{n,m}) - \boldsymbol{g}^{\varepsilon}(\boldsymbol{x}^2_{n,m})\right|^2 \\
&+ \sum_{n=1}^{\widetilde{N}}\sum_{m=1}^{\widetilde{M}} \left|\alpha\boldsymbol{u}_{NM}(\boldsymbol{a}^1, \boldsymbol{a}^2, \boldsymbol{b}^1, \boldsymbol{b}^2, \boldsymbol{c}^1, \boldsymbol{c}^2, \boldsymbol{\xi}^1, \boldsymbol{\xi}^2; \boldsymbol{x}^2_{n,m}) + (1-\alpha)\boldsymbol{t}_{NM}(\boldsymbol{a}^1, \boldsymbol{a}^2, \boldsymbol{b}^1, \boldsymbol{b}^2, \boldsymbol{c}^1, \boldsymbol{c}^2, \boldsymbol{\xi}^1, \boldsymbol{\xi}^2; \boldsymbol{x}^2_{n,m})\right|^2 \\
&+ \lambda_1\left\{|\boldsymbol{a}^1|^2 + |\boldsymbol{a}^2|^2 + |\boldsymbol{b}^1|^2 + |\boldsymbol{b}^2|^2 + |\boldsymbol{c}^1|^2 + |\boldsymbol{c}^2|^2\right\} \\
&+ \lambda_2\left[\sum_{n=1}^{N}\sum_{m=2}^{M}\left(\frac{r_{n,m} - r_{n,m-1}}{2\pi/M}\right)^2 + \sum_{n=2}^{N}\sum_{m=1}^{M}\left(\frac{r_{n,m} - r_{n-1,m}}{\pi/(N+1)}\right)^2\right],
\end{aligned} \tag{14}$$

where $\lambda_1, \lambda_2 \geq 0$ are regularization parameters to be prescribed and $\boldsymbol{\eta} = [\eta_{int}, \eta_{ext}]$.

Remarks.

(i) The Dirichlet data (1b) and the traction data (1d) come from practical measurements which are inherently contaminated with noisy errors, and that is why we have replaced $\boldsymbol{f}$ and $\boldsymbol{g}$ by $\boldsymbol{f}^{\varepsilon} = \left[f_1^{\varepsilon}, f_2^{\varepsilon}, f_3^{\varepsilon}\right]^{\mathsf{T}}$ and $\boldsymbol{g}^{\varepsilon} = \left[g_1^{\varepsilon}, g_2^{\varepsilon}, g_3^{\varepsilon}\right]^{\mathsf{T}}$, respectively, where, in computation, the noisy data are generated as

$$f_\ell^{\varepsilon}(\boldsymbol{x}_{n,m}^2) = (1 + \rho_{n,m}\, p_f)\, f_\ell(\boldsymbol{x}_{n,m}^2), \quad g_\ell^{\varepsilon}(\boldsymbol{x}_{n,m}^2) = (1 + \rho_{n,m}\, p_g)\, g_\ell(\boldsymbol{x}_{n,m}^2), \quad n = \overline{1, \widetilde{N}},\ m = \overline{1, \widetilde{M}}, \tag{15}$$

where p_f and p_g represent the percentage of noise added to the Dirichlet and Neumann boundary data on $\partial\Omega_2$, respectively, and $\rho_{m,n}$ is a pseudo-random noisy variable drawn from a uniform distribution in $[-1, 1]$ using the MATLAB© command `-1+2*rand(1,`$\widetilde{M}\widetilde{N}$`)`. In our numerical experiments it was observed that the effect of noise added to the Dirichlet boundary data was similar to that of perturbing the Neumann data. As a result in the numerical results section we only present results for noisy Neumann data, i.e. $p_g \neq 0$ and $p_f = 0$. In Section 5 we shall re-denote p_g by p.

(ii) For $\partial\Omega_2$ a sphere, the outward normal vector $\boldsymbol{n}$ is defined as follows:

$$\boldsymbol{n} = (\sin\vartheta\cos\phi,\, \sin\vartheta\sin\phi,\, \cos\vartheta) \quad \text{on} \quad \partial\Omega_2\,. \tag{16}$$

In the case of the boundary $\partial\Omega_1$, we know that the position vector of a boundary point is given by

$$\boldsymbol{x}^1(\vartheta, \phi) = (X, Y, Z) + r(\vartheta, \phi)\,(\sin\vartheta\cos\phi, \sin\vartheta\sin\phi, \cos\vartheta)\,, \tag{17}$$

and that the normal to the parametrised surface is given by

$$\boldsymbol{n} = \frac{\boldsymbol{x}_\vartheta^1 \times \boldsymbol{x}_\phi^1}{|\boldsymbol{x}_\vartheta^1 \times \boldsymbol{x}_\phi^1|}, \tag{18}$$

where the subscripts $_\vartheta$ and $_\phi$ denote the partial derivatives with respect to ϑ and ϕ, respectively. Now,

$$\boldsymbol{x}_\vartheta^1 = [r_\vartheta \sin\vartheta\cos\phi + r\cos\vartheta\cos\phi,\, r_\vartheta \sin\vartheta\sin\phi + r\cos\vartheta\sin\phi,\, r_\vartheta\cos\vartheta - r\sin\vartheta]\,,$$

$$\boldsymbol{x}_\phi^1 = [r_\phi \sin\vartheta\cos\phi - r\sin\vartheta\sin\phi,\, r_\phi \sin\vartheta\sin\phi + r\sin\vartheta\cos\phi,\, r_\phi\cos\vartheta]\,,$$

and thus

$$\boldsymbol{x}_\vartheta^1 \times \boldsymbol{x}_\phi^1 = -r\,\big[-r_\phi\sin\phi + r_\vartheta\sin\vartheta\cos\vartheta\cos\phi - r\sin^2\vartheta\cos\phi,$$

$$r_\phi\cos\phi + r_\vartheta\sin\vartheta\cos\vartheta\sin\phi - r\sin^2\vartheta\sin\phi,\, -\sin\vartheta(r_\vartheta\sin\vartheta + r\cos\vartheta)\big]\,,$$

and

$$|\boldsymbol{x}^1_\vartheta \times \boldsymbol{x}^1_\phi| = r\sqrt{(r^2 + r^2_\vartheta)\sin^2\vartheta + r^2_\phi} \tag{19}$$

yielding

$$\boldsymbol{n} = \frac{1}{\sqrt{(r^2 + r^2_\vartheta)\sin^2\vartheta + r^2_\phi}}\big[-r_\phi \sin\phi + r_\vartheta \sin\vartheta\cos\vartheta\cos\phi - r\sin^2\vartheta\cos\phi,$$
$$r_\phi\cos\phi + r_\vartheta\sin\vartheta\cos\vartheta\sin\phi - r\sin^2\vartheta\sin\phi,\ -\sin\vartheta(r_\vartheta\sin\vartheta + r\cos\vartheta)\big] \quad \text{on} \quad \partial\Omega_1\,. \tag{20}$$

As a result, in the expressions for the tractions (6) the normal derivatives are given by (16) and (20) for $\boldsymbol{x} \in \partial\Omega_2$ and $\boldsymbol{x} \in \partial\Omega_1$, respectively. In (20), we use the finite-difference approximations

$$r_\phi(\vartheta_n, \phi_m) \approx \frac{r_{n,m+1} - r_{n,m-1}}{4\pi/M}, \quad n = \overline{1, N},\ m = \overline{1, M}, \tag{21}$$

with the convention that $r_{n,M+1} = r_{n,1}$, $r_{n,0} = r_{n,M}$, and

$$r_\vartheta(\vartheta_n, \phi_m) \approx \frac{r_{n+1,m} - r_{n-1,m}}{2\pi/(N+1)},\ n = \overline{2, N-1},$$

$$r_\vartheta(\vartheta_1, \phi_m) \approx \frac{-r_{3,m} + 4r_{2,m} - 3r_{1,m}}{2\pi/(N+1)}, \quad r_\vartheta(\vartheta_N, \phi_m) \approx \frac{r_{N-2,m} - 4r_{N-1,m} + 3r_{N,m}}{2\pi/(N+1)}, \quad m = \overline{1, M}. \tag{22}$$

(iii) Since the total number of unknowns is $7NM+5$ and the number of boundary condition collocation equations is $3NM + 6\widetilde{N}\widetilde{M}$ we need to take $\widetilde{N}\widetilde{M} \geq 2NM/3 + 1$.

(iv) Since the inverse problem is ill-posed, in (14), the regularization terms $\lambda_1\big\{|\boldsymbol{a}^1|^2 + |\boldsymbol{a}^2|^2 + |\boldsymbol{b}^1|^2 + |\boldsymbol{b}^2|^2 + |\boldsymbol{c}^1|^2 + |\boldsymbol{c}^2|^2\big\}$ and $\lambda_2\big(|r_\vartheta|^2 + |r_\phi|^2\big)$ are added in order to achieve the stability of the numerical MFS solution u_{NM} and the smooth boundary $\partial\Omega_1$. We do not include regularization terms $\lambda_3|\boldsymbol{\eta}|^2$ and $\lambda_4|\boldsymbol{C}|^2$ since both $\boldsymbol{\eta}$ and $\boldsymbol{C}$ only have a small number of components and the numerical solution is expected to be stable in both $\boldsymbol{\eta}$ and $\boldsymbol{C}$.

4.1 Non-linear minimization

The minimization of functional (14) is carried out using the MATLAB© [32] optimization toolbox routine `lsqnonlin` which solves nonlinear least squares problems. This routine by default uses the so-called trust-region-reflective algorithm based on the interior-reflective Newton method [13, 14], and terminates when (i) the change

in the solution vector is less than a specified tolerance, or (ii) the change in the residual is less than a specified tolerance, or (iii) the specified number of iterations or number of function evaluations is exceeded. The routine `lsqnonlin` does not require the user to provide the gradient and, in addition, it offers the option of imposing lower and upper bounds on the elements of the vector of unknowns $(\boldsymbol{a}^1, \boldsymbol{a}^2, \boldsymbol{b}^1, \boldsymbol{b}^2, \boldsymbol{c}^1, \boldsymbol{c}^2, \boldsymbol{r}, \boldsymbol{\eta}, \boldsymbol{C})$ through the vectors `lb` and `up`. We can thus easily impose the constraints $0 < r_{n,m} < 1, \quad n = \overline{1,N}, m = \overline{1,M}, 0 < \eta_{int} < 1, 1 < \eta_{ext} < S$ and $-R < X < R, -R < Y < R, -R < Z < R$. In our numerical experiments we choose $S = 6$. Moreover, we choose the initial guess vector of unknowns $(\boldsymbol{a}_0^1, \boldsymbol{a}_0^2, \boldsymbol{b}_0^1, \boldsymbol{b}_0^2, \boldsymbol{c}_0^1, \boldsymbol{c}_0^2, \boldsymbol{r}_0, \eta_{int}^0, \eta_{ext}^0, \boldsymbol{C}) = (\mathbf{0}, \mathbf{0}, \mathbf{0}, \mathbf{0}, \mathbf{0}, \mathbf{0}, \mathbf{0.3}, 0.2, 3, \mathbf{0})$.

5 Numerical examples

In all numerical examples considered in this section we took $\mu = 1$ and $\nu = 0.3$. In all figures presented the reconstructed values of $\boldsymbol{r}$, i.e. the numerically reconstructed object Ω_1, are presented as red colour dots.

5.1 Example 1 (Rigid inclusion)

We consider an example in a hollow sphere domain $\Omega = \Omega_2 \backslash \Omega_1$, where

$$\Omega_2 = \left\{(x_1, x_2, x_3) \in \mathbb{R}^3 \mid x_1^2 + x_2^2 + x_3^2 < r_o^2\right\}, \tag{23}$$

$$\Omega_1 = \left\{(x_1, x_2, x_3) \in \mathbb{R}^3 \mid x_1^2 + x_2^2 + x_3^2 < r_{int}^2\right\}, \quad 0 < r_{int} < r_o = R = 1. \tag{24}$$

We consider the following exact solutions for the displacements

$$u_\ell(x_1, x_2, x_3) = \left[A + \frac{B}{(x_1^2 + x_2^2 + x_3^2)^{3/2}}\right] x_\ell, \quad \ell = 1, 2, 3, \quad (x_1, x_2, x_3) \in \overline{\Omega}, \tag{25}$$

where A and B are constants chosen such that $u_1 = u_2 = u_3 = 0$, on the inner boundary. We choose $A = 1$ and $B = -0.125$ so that the internal sphere has radius $r_{int} = 0.5$.

In Figures 1-3 we present the results obtained with no noise, no regularization with $M = N = 6, \widetilde{M} = \widetilde{N} = 8$, $M = N = 8, \widetilde{M} = \widetilde{N} = 10$, $M = N = 10, \widetilde{M} = \widetilde{N} = 12$, respectively, for various numbers of iterations (`iter`), as well as the correct sphere (24) to be reconstructed. From these figures it can be seen that, for exact data, very accurate numerical results are obtained in a relatively small number of iterations. Another indicator of the

accuracy of the method is the maximum radii deviation

$$E_r = \max_{n=\overline{1,N},m=\overline{1,M}} |r_{n,m} - r_{int}|.$$

In Figure 4 we present the variation of E_r for $M = N = 6, \widetilde{M} = \widetilde{N} = 8$, $M = N = 8, \widetilde{M} = \widetilde{N} = 10$, $M = N = 10, \widetilde{M} = \widetilde{N} = 12$, respectively, for various numbers of iterations.

5.2 Example 2 (Cavity)

We consider again the domain $\Omega = \Omega_2 \backslash \Omega_1$ where Ω_2 and Ω_1 are spheres defined by (23) and (24), respectively. The exact solution has the form (25) but now, in order to have $t_1 = t_2 = t_3 = 0$, on the inner boundary we need to choose the constants A and B differently. In particular, we choose $A = 1$ and $B = 0.0625(1 + \nu)/(1 - 2\nu)$ so that the internal sphere has radius $r_{int} = 0.5$.

In Figures 5-7 we present the results obtained with no noise, no regularization with $M = N = 6, \widetilde{M} = \widetilde{N} = 8$, $M = N = 8, \widetilde{M} = \widetilde{N} = 10$, $M = N = 10, \widetilde{M} = \widetilde{N} = 12$, respectively, for various numbers of iterations, as well as the correct sphere (24) to be reconstructed. From this figure it can be seen that, for exact data, very accurate numerical results are obtained in a relatively small number of iterations. In Figure 8 we present the variation of E_r for $M = N = 6, \widetilde{M} = \widetilde{N} = 8$, $M = N = 8, \widetilde{M} = \widetilde{N} = 10$, $M = N = 10, \widetilde{M} = \widetilde{N} = 12$, respectively, for various numbers of iterations.

5.3 Example 3

We next consider the case $R = 1$, $\alpha = 1$ and the rigid inclusion Ω_1 has an acorn shape [23, 36] described parametrically by

$$r(\vartheta, \phi) = 0.2 \left(0.6 + \sqrt{4.25 + 2\cos 3\vartheta}\right), \qquad \vartheta \in (0, \pi),\ \phi \in [0, 2\pi), \tag{26}$$

and Ω_2 is the unit sphere. The Dirichlet data on $\partial\Omega_2$ is taken as

$$u_\ell(x_1, x_2, x_3) = \left[1 - \frac{2}{\left(x_1^2 + x_2^2 + x_3^2\right)^{3/2}}\right] x_\ell, \quad \ell = 1, 2, 3, \qquad (x_1, x_2, x_3) \in \partial\Omega_2. \tag{27}$$

Since in this case no analytical solution is available, the Neumann data (1d) is numerically simulated by solving the direct Dirichlet well-posed problem given by equations (1a), (1b), and (1c) with $\alpha = 1$, when $\partial\Omega_1$ is given by (26), using the MFS with $M = N = 20, \widetilde{M} = \widetilde{N} = 16$. In order to avoid committing an inverse crime, the inverse solver is applied using $M = N = 8, \widetilde{M} = \widetilde{N} = 10$.

In Figures 9 and 10 we present the results obtained with $X = Y = Z = 0.1$, no noise and $p = 5\%$ noise, respectively, no regularization with $M = N = 8, \widetilde{M} = \widetilde{N} = 10$, for various numbers of iterations, as well as the correct shape (26) to be reconstructed. From Figure 9 it can be seen that for exact data, accurate retrievals of the acorn shape (26) are obtained as the number of iterations increase, but this conclusion is not maintained for noisy data, see Figure 10. This is because, in the absence of regularization, the obtained numerical solution will amplify the small noise with which the input data is contaminated, thus becoming unstable. In order to deal with this instability, regularization should be included.

In Figures 11 and 12 we present the results obtained with noise $p = 5\%$ after 100 iterations, and regularization with λ_1 (with $\lambda_2 = 0$) and λ_2 (with $\lambda_1 = 0$), respectively. From Figure 11 it can be seen that regularization with λ_1 is not very effective and better results are obtained for regularization with λ_2, in particular when λ_2 is about 10^{-1}, see Figure 12.

Similar results have been obtained for reconstructing an acorn shape cavity, i.e. $\alpha = 0$, and are therefore not presented.

5.4 Example 4

We finally consider the case $R = 1$, $\alpha = 1$ and the rigid inclusion Ω_1 is a pinched ball [23, 36] described parametrically by

$$r(\vartheta, \phi) = 0.4\sqrt{1.44 + 0.5(\cos 2\vartheta - 1)\cos 2\phi}, \qquad \vartheta \in (0, \pi),\ \phi \in [0, 2\pi), \tag{28}$$

and Ω_2 is the unit sphere. The Dirichlet data on $\partial\Omega_2$ is taken as in (27).

Since in this case no analytical solution is available, the Neumann data (1d) is numerically simulated by solving the direct Dirichlet well-posed problem given by equations (1a), (1b), and (1c) with $\alpha = 1$, when $\partial\Omega_1$ is given by (28), using the MFS with $M = N = \widetilde{M} = \widetilde{N} = 20$. In order to avoid committing an inverse crime, the inverse solver is applied using $M = N = 8, \widetilde{M} = \widetilde{N} = 10$.

In Figures 13 and 14 we present the results obtained with $X = Y = Z = 0$, no noise and $p = 5\%$ noise, respectively, no regularization with $M = N = 8, \widetilde{M} = \widetilde{N} = 10$, for various numbers of iterations, as well as the correct shape (28) to be reconstructed. The same conclusions as those discussed for Example 3 from Figures 9 and 10 above can be drawn from Figures 13 and 14 for Example 4.

In Figures 15 and 16 we present the results obtained with noise $p = 5\%$ after 100 iterations, and regularization

with λ_1 (with $\lambda_2 = 0$) and λ_2 (with $\lambda_1 = 0$), respectively. Finally, in Figure 17 we present the corresponding L-curves with λ_1 and λ_2 regularizations for noise $p = 5\%$ after 100 iterations. The L-curve corner for regularization in λ_1 is not consistent with the best results which appear just above $\lambda_1 = 10^{-1}$ in Figure 15 whereas the L-curve corner for regularization in λ_2 is consistent with the the best results which appear around $\lambda_2 = 10^{-1}$ in Figure 16.

6 Conclusions

The main features of this work can be summarized as follows:

- This is the first time a three-dimensional inverse geometric problem in elasticity has been considered using the MFS.
- We get the full benefits of the MFS since we are dealing with a nonlinear problem in three dimensions and in complex geometries. Here, the meshlessness and the boundary nature of the method and their concomitant ease of implementation become important.
- The numerical results indicate that the numerical method is accurate (for no noise) and stable with respect to noise added in the input data.
- Accurate results are obtained for relatively few degrees of freedom.
- The dynamic approach of the MFS has been used. It is well-suited for such nonlinear problems since, in addition to the parameters determining the shape of the sought void, we simultaneously determine the location of the unknown pseudo-boundaries as well as the coordinates of the centre of the object.
- The MFS implementations to three-dimensional isotropic linear thermo-elasticity, as well as to two- and three-dimensional anisotropic linear elasticity, of the corresponding inverse void problems are deferred to a future work.

Acknowledgements. Liviu Marin acknowledges the financial support received from the Romanian National Authority for Scientific Research (CNCS–UEFISCDI), project number PN–II–ID–PCE–2011–3–0521.

References

[1] G. Alessandrini, A. Bilotta, G. Formica, A. Morassi, E. Rosset, and E. Turco, *Numerical size estimates of inclusions in elastic bodies*, Inverse Problems **21** (2005), 133–151.

[2] G. Alessandrini, A. Morassi, and E. Rosset, *Detecting an inclusion in an elastic body by boundary measurement*, SIAM J. Math. Anal. **33** (2002), 1247–1268.

[3] C. J. S. Alves and N. F. M. Martins, *The direct method of fundamental solutions and the inverse Kirsch-Kress method for the reconstruction of elastic inclusions or cavities*, J. Integral Equations Appl. **21** (2009), 153–178.

[4] D. D. Ang, D. D. Trong, and M. Yamamoto, *Identification of cavities inside two-dimensional heterogeneous isotropic elastic bodies*, J. Elasticity **56** (1999), 199–212.

[5] P. K. Banerjee and R. Butterfield, *Boundary Element Methods in Engineering Science*, McGraw-Hill Book Co. (UK), Ltd., London-New York, 1981.

[6] M. R. Barone and R. J. Yang, *A boundary element approach for recovery of shape sensitivities in three-dimensional elastic solids*, Comput. Methods Appl. Mech. Engrg. **74** (1989), 69–82.

[7] H. Ben Ameur, M. Burger, and B. Hackl, *Level set methods for geometric inverse problems in linear elasticity*, Inverse Problems **20** (2004) 673–696.

[8] H. Ben Ameur, M. Burger, and B. Hackl, *Cavity identification in linear elasticity and thermoelasticity*, Math. Methods Appl. Sci. **3** (2007), 625–647.

[9] L. M. Bezerra and S. A. Saigal, *Boundary element formulation for the inverse elastostatics problem (IESP) of flaw detection*, Internat. J. Numer. Methods Engrg. **36** (1993), 2189–2202.

[10] M. Bonnet and A. Constantinescu, *Inverse problems in elasticity*, Inverse Problems **21** (2005), R1–R50.

[11] M. Bonnet and B. J. Guzina, *Elastic-wave identification of penetrable obstacles using shape-material sensitivity framework*, J. Comput. Phys. **228** (2009), 294–311.

[12] D. Borman, D. B. Ingham, B. T. Johansson, and D. Lesnic, *The method of fundamental solutions for detection of cavities in EIT*, J. Integral Equations Appl. **21** (2009), 381–404.

[13] T. F. Coleman and Y. Li, *On the convergence of interior-reflective Newton methods for nonlinear minimization subject to bounds*, Math. Programming **67** (1994), 189–224.

[14] T. F. Coleman and Y. Li, *An interior trust region approach for nonlinear minimization subject to bounds*, SIAM J. Optim. **6** (1996), 418–445.

[15] P. Gorzelańczyk and J. A. Kołodziej, *Some remarks concerning the shape of the source contour with application of the method of fundamental solutions to elastic torsion of prismatic rods*, Eng. Anal. Bound. Elem. **37** (2008), 64–75.

[16] J. Hadamard, *Lectures on Cauchy Problem in Linear Partial Differential Equations*. Yale University Press, New Haven, 1923.

[17] F. Hartmann, *Elastostatics*, Progress in Boundary Element Methods. Vol. 1 (C. A. Brebbia, ed.), Pentech Press, London, 1981, pp. 84–167.

[18] S.-C. Hsieh and T. Mura, *Nondestructive cavity identification in structures*, Int. J. Solids Struct. **30** (1993), 1579–1587.

[19] M. Ikehata and H. Itou, *Extracting the support function of a cavity in an isotropic elastic body from a single set of boundary data*, Inverse Problems **25** (2009), 105005.

[20] A. Karageorghis, D. Lesnic, and L. Marin, *A survey of applications of the MFS to inverse problems*, Inverse Probl. Sci. Eng. **19** (2011), 309–336.

[21] A. Karageorghis, D. Lesnic, and L. Marin, *The method of fundamental solutions for the detection of rigid inclusions and cavities in plane linear elastic bodies*, Comput. & Structures **106-107** (2012), 176–188.

[22] A. Karageorghis, D. Lesnic, and L. Marin, *A moving pseudo-boundary method of fundamental solutions for void detection*, Numer. Methods Partial Differential Equations **29** (2013), 935–960.

[23] A. Karageorghis, D. Lesnic, and L. Marin, *A moving pseudo-boundary MFS for three-dimensional void detection*, Adv. Appl. Math. Mech. **5** (2013), 510–527.

[24] A. J. Kassab, F. A. Moslehy, and A. B. Daryapurkar, *Nondestructive detection of cavities by an inverse elastostatics boundary element method*, Eng. Anal. Bound. Elem. **13** (1994), 45–55.

[25] A. Kirsch and R. Kress, *On an integral equation of the first kind in inverse acoustic scattering*, Int. Ser. Numer. Math. **77** (1986), 93–102.

[26] V. D. Kupradze and M. A. Aleksidze, *The method of functional equations for the approximate solution of certain boundary value problems*, Comput. Math. Math. Phys. **4** (1964), 82–126.

[27] D. Lesnic, J. R. Berger, and P. A. Martin, *A boundary element regularization method for the boundary determination in potential corrosion damage*, Inverse Probl. Eng. **10** (2002), 163–182.

[28] L. Marin, *Regularized method of fundamental solutions for boundary identification in two-dimensional isotropic linear elasticity*, Int. J. Solids Struct. **47** (2010), 3326–3340.

[29] L. Marin, and D. Lesnic, *BEM first-order regularisation method in linear elasticity for boundary identification*, Comput. Methods Appl. Mech. Engrg. **192** (2003), 2059–2071.

[30] S. C. Mellings and M. H. Aliabadi, *Flaw identification using the boundary element method*, Internat. J. Numer. Methods Engrg. **38** (1995), 399–419.

[31] R. Mathon and R. L. Johnston, *The approximate solution of elliptic boundary value problems by fundamental solutions*, SIAM J. Numer. Anal. **14** (1977), 638–650.

[32] The MathWorks, Inc., 3 Apple Hill Dr., Natick, MA, *Matlab*.

[33] A. Morassi and E. Rosset, *Detecting rigid inclusions, or cavities, in an elastic body*, J. Elasticity **73** (2003), 101–126.

[34] A. Morassi and E. Rosset, *Uniqueness and stability in determining a rigid inclusion in an elastic body*, Mem. Amer. Math. Soc. **200** (2009), 58pp.

[35] A. Poullikkas, A. Karageorghis, and G. Georgiou, *The method of fundamental solutions for three-dimensional elastostatics problems*, Comput. & Structures **80** (2002), 365–370.

[36] P. Serranho, *A hybrid method for inverse scattering for sound-soft obstacles in* $\mathbb{R}^3$, Inverse Probl. Imaging **1** (2007), 691–712.

[37] T. W. Ulrich, F. A. Moslehy, and A. J. Kassab, *A BEM based pattern search solution for a class of inverse elastostatic problems*, Int. J. Solids Struct. **33** (1996), 2123–2131.

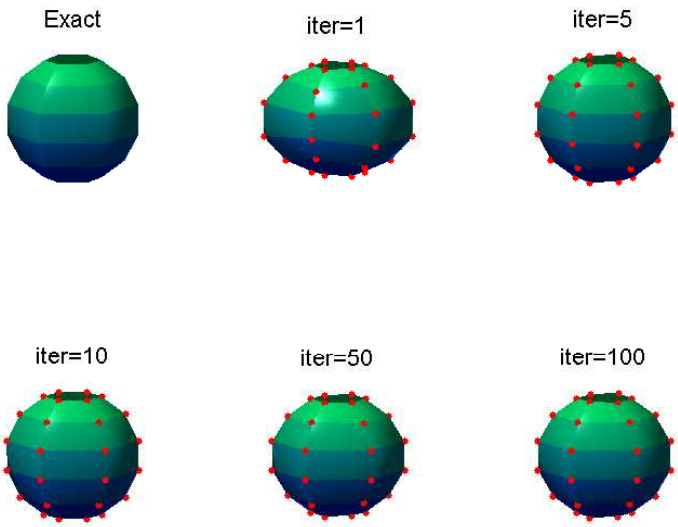

Figure 1: Example 1: Results for $M = N = 6, \widetilde{M} = \widetilde{N} = 8$, no noise and no regularization.

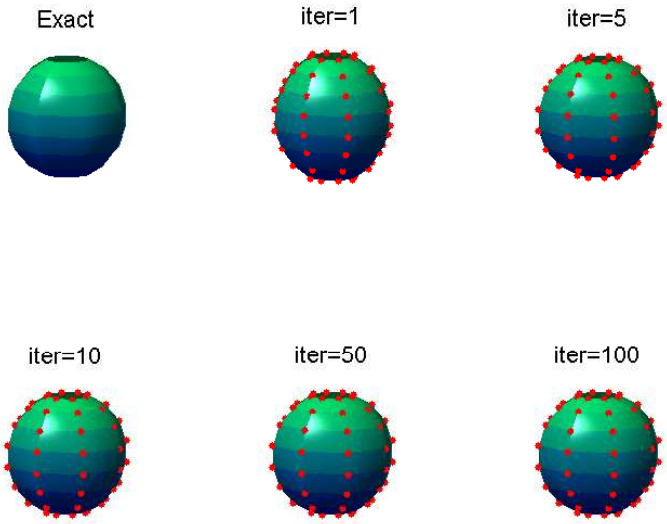

Figure 2: Example 1: Results for $M = N = 8, \widetilde{M} = \widetilde{N} = 10$, no noise and no regularization.

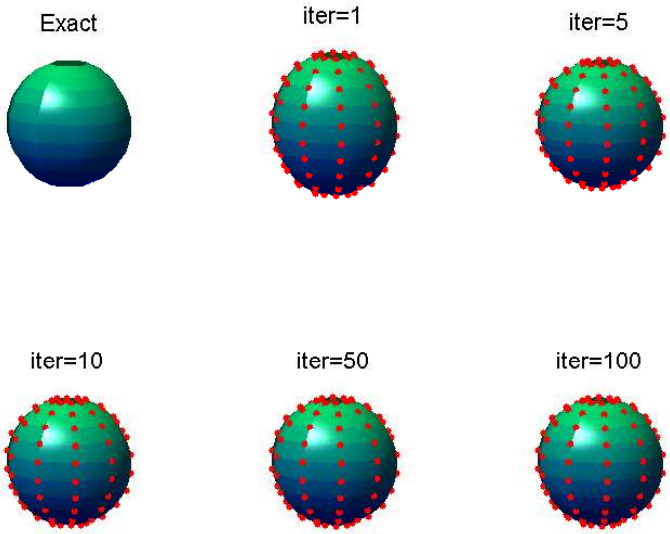

Figure 3: Example 1: Results for $M = N = 10, \widetilde{M} = \widetilde{N} = 12$, no noise and no regularization.

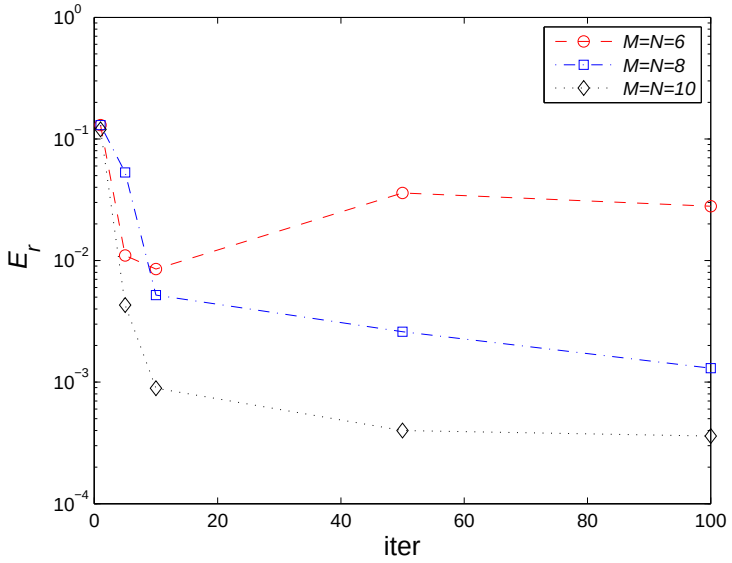

Figure 4: Example 1: Variation of error E_r with the number of iterations.

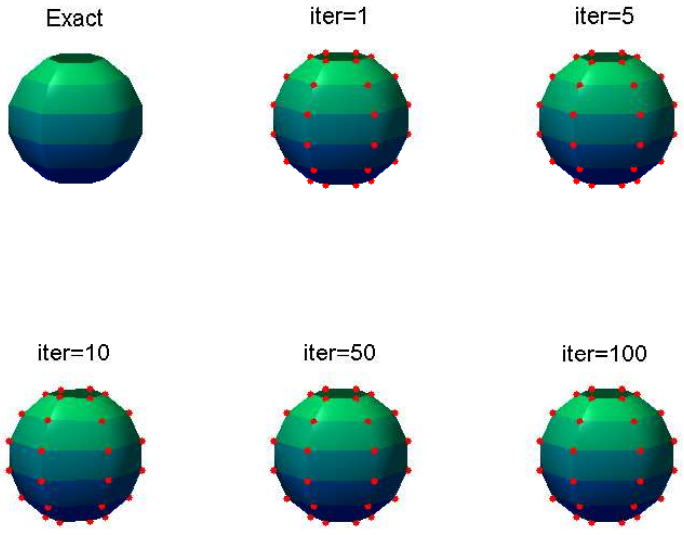

Figure 5: Example 2: Results for $M = N = 6, \widetilde{M} = \widetilde{N} = 8$, no noise and no regularization.

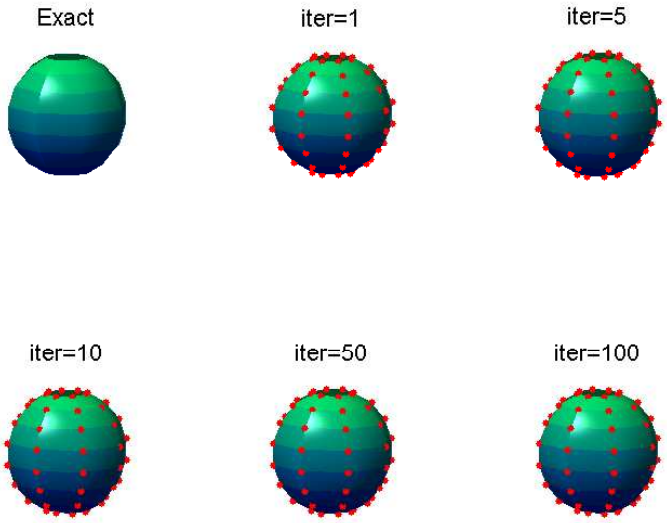

Figure 6: Example 2: Results for $M = N = 8, \widetilde{M} = \widetilde{N} = 10$, no noise and no regularization.

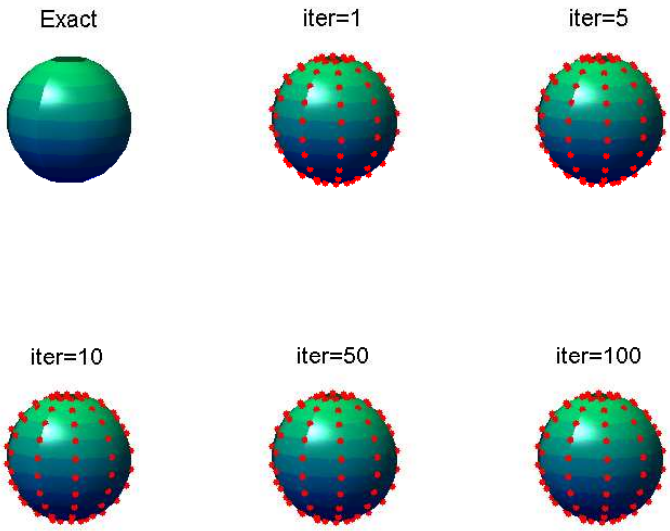

Figure 7: Example 2: Results for $M = N = 10, \widetilde{M} = \widetilde{N} = 12$, no noise and no regularization.

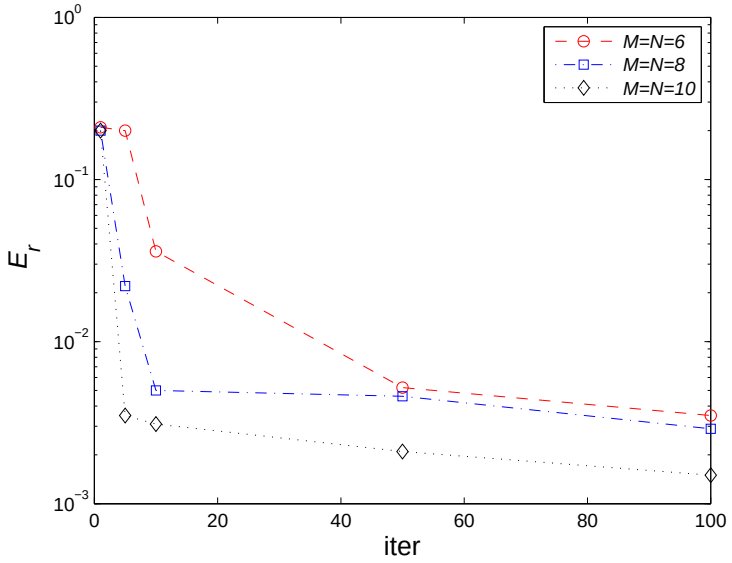

Figure 8: Example 2: Variation of error E_r with the number of iterations.

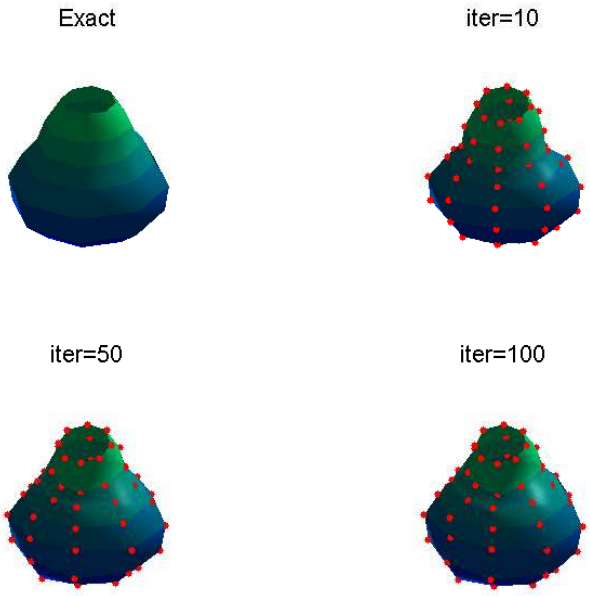

Figure 9: Example 3: Results for $M = N = 8, \widetilde{M} = \widetilde{N} = 10$, no noise and no regularization.

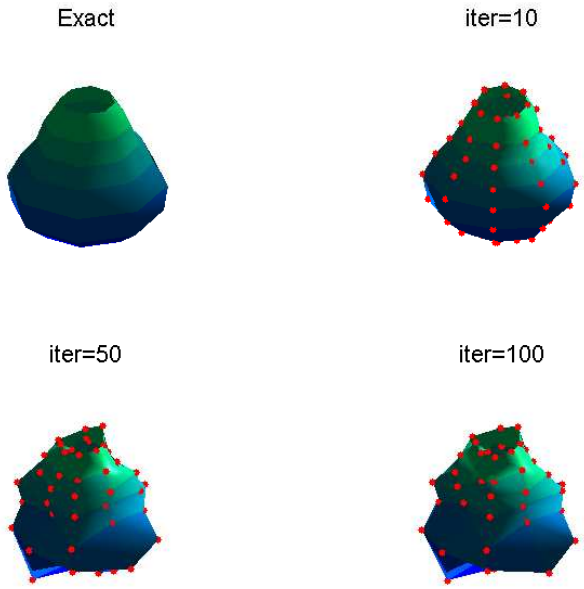

Figure 10: Example 3: Results for $M = N = 8, \widetilde{M} = \widetilde{N} = 10$, noise $p = 5\%$ and no regularization.

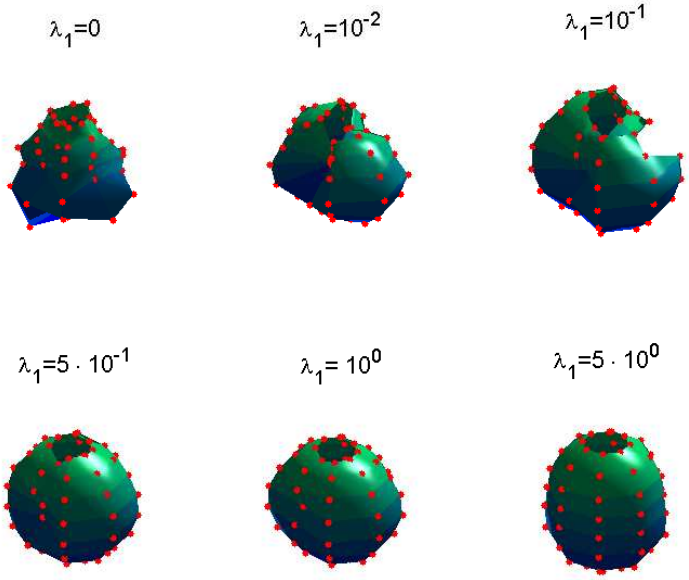

Figure 11: Example 3: Results for $M = N = 8, \widetilde{M} = \widetilde{N} = 10$, noise $p = 5\%$ and regularization with λ_1.

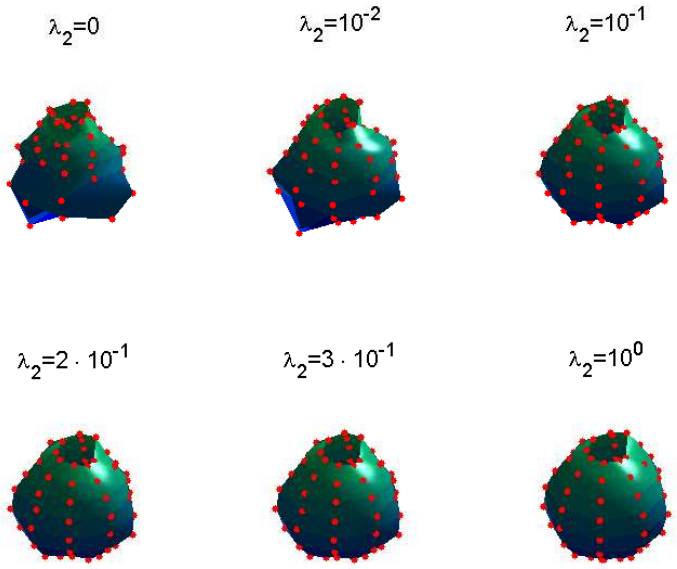

Figure 12: Example 3: Results for $M = N = 8, \widetilde{M} = \widetilde{N} = 10$, noise $p = 5\%$ and regularization with λ_2.

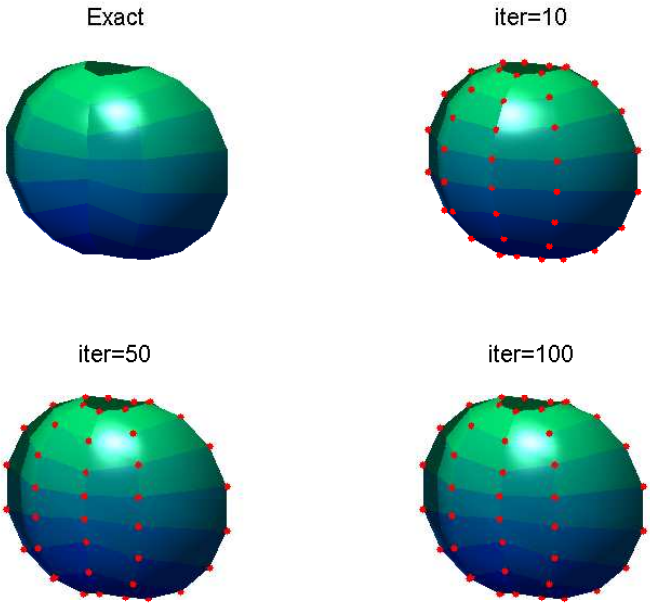

Figure 13: Example 4: Results for $M = N = 8, \widetilde{M} = \widetilde{N} = 10$, no noise and no regularization.

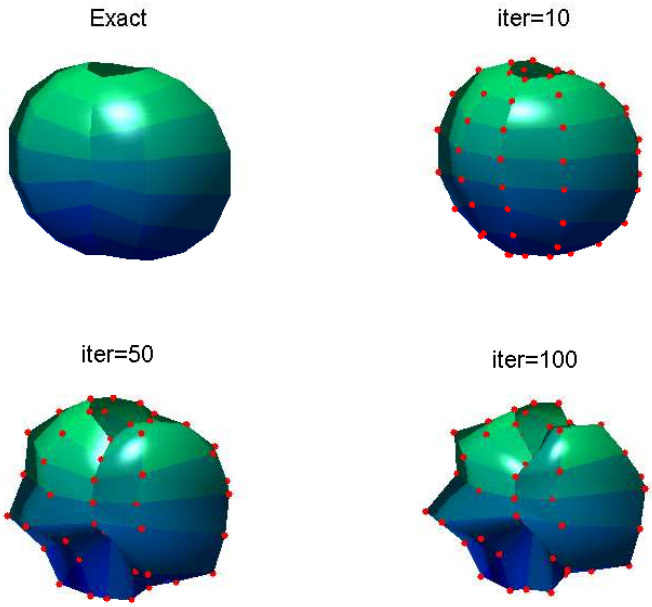

Figure 14: Example 4: Results for $M = N = 8, \widetilde{M} = \widetilde{N} = 10$, noise $p = 5\%$ and no regularization.

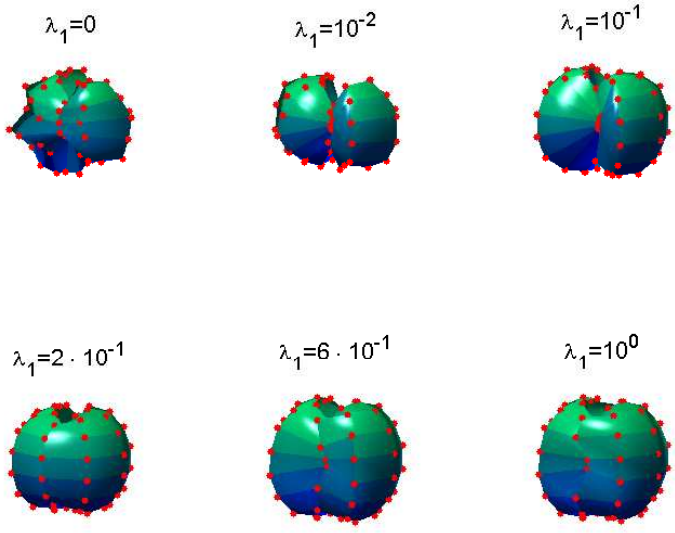

Figure 15: Example 4: Results for $M = N = 8, \widetilde{M} = \widetilde{N} = 10$, noise $p = 5\%$ and regularization with λ_1.

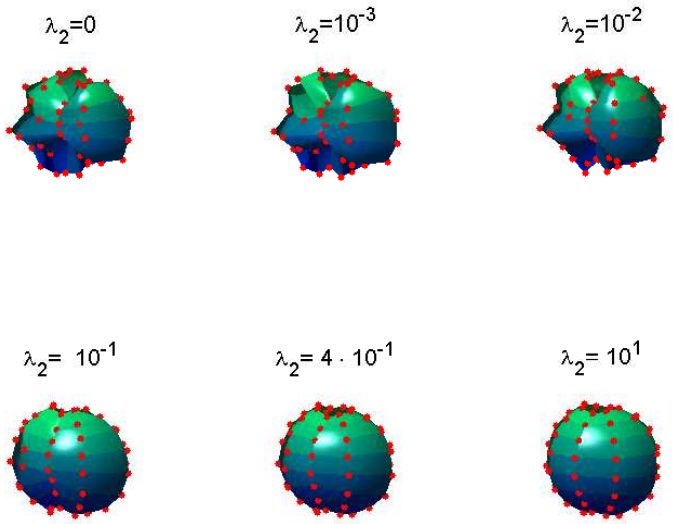

Figure 16: Example 4: Results for $M = N = 8, \widetilde{M} = \widetilde{N} = 10$, noise $p = 5\%$ and regularization with λ_2.

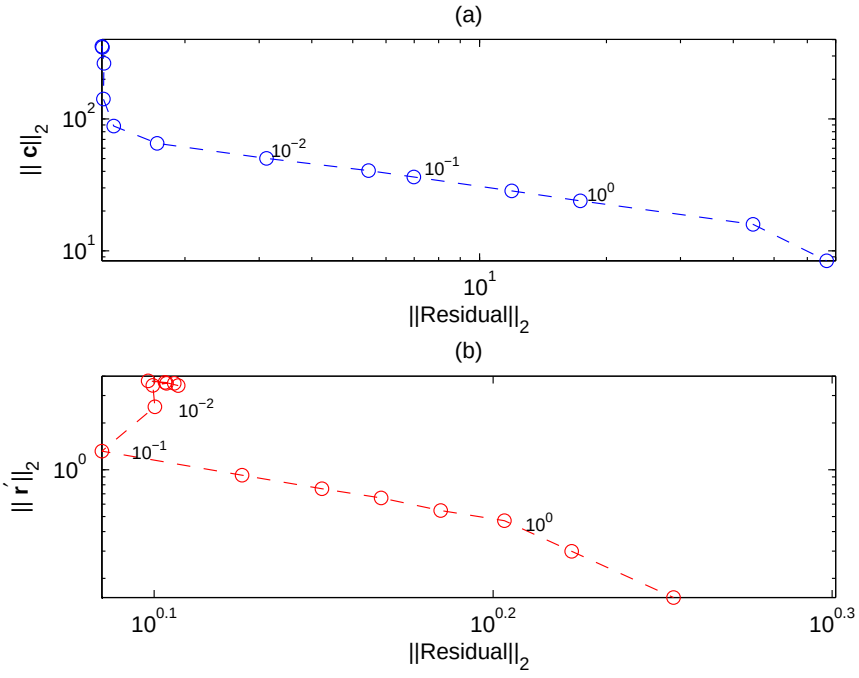

Figure 17: Example 4: L-curves obtained with regularization in (a) λ_1 and (b) λ_2 for noise $p = 5\%$.